Single channel frequency diverse computational imaging system for through-the-wall sensing

Alvarez Narciandi, G., Garcia-Fernandez, M., & Yurduseven, O. (2024). Single channel frequency diverse computational imaging system for through-the-wall sensing. *IEEE Transactions on Geoscience and Remote Sensing*, *62*, Article 5105110. Advance online publication. https://doi.org/10.1109/TGRS.2024.3383569

Published in:
IEEE Transactions on Geoscience and Remote Sensing

Document Version:
Peer reviewed version

Single Channel Frequency Diverse Computational Imaging System for Through-the-Wall Sensing

María García-Fernández, *Member, IEEE,* Guillermo Álvarez-Narciandi, *Member, IEEE,* and Okan Yurduseven, *Senior Member, IEEE*

***Abstract*—This paper presents a through-the-wall computational imaging (CI) system employing frequency-diverse antennas. CI has emerged as a promising alternative to conventional radar imaging systems (such as those based on synthetic aperture radar) since they allow to significantly reduce the acquisition time and the hardware complexity. CI relies on using compressive antennas, radiating quasi-orthogonal radiation patterns, to compress the scene information into a single channel (or a reduced number of them). The feasibility of performing through-the-wall sensing employing frequency-diverse antennas is demonstrated for the first time in this work. Furthermore, a method to account for the propagation through the wall, which helps to increase the quality of the reconstructed images, is also proposed. Measurement results show that the system can successfully image targets hidden behind a wall with only a single standalone acquisition, thus drastically reducing the inspection time.**

***Index Terms*—frequency diverse antennas; computational imaging; through-the-wall imaging; radar.**

I. Introduction

ELECTROMAGNETIC waves can propagate through multiple optically opaque materials, making electromagnetic imaging of great interest for a wide range of applications [1]. In particular, electromagnetic imaging at microwave and millimeter-wave frequency bands has been used in the context of security and defense applications for people screening [2], [3], [4], [5] and landmine detection [6], [7], [8], [9], in the field of non-destructive evaluation (NDE) [10], [11], [12], and for medical diagnosis [13], [14] among other fields. Active electromagnetic imaging systems illuminate the scene under investigation with electromagnetic waves and capture the signals backscattered by it. Most of these systems are based on synthetic aperture radar (SAR) techniques, which enable to bypass the need of a big physical aperture to achieve a good cross-range resolution. Instead, SAR-based systems rely on combining measurements acquired at different positions to synthetically increase the cross-range resolution of the obtained images [2]. This usually involves moving a single transmitter (TX) - receiver (RX) pair according to a given acquisition grid over the scene under investigation using mechanical positioners, making the overall system bulky and entailing long acquisition times. The use of multiple TX-RX pairs and multiple-input multiple-output (MIMO) configurations has been adopted to reduce the acquisition time of these systems [3]. Moreover, recently a great research effort has been devoted to the development of imaging systems taking advantadge of flexible moving platforms, such as unmanned aerial vehicles (UAVs) [8], [9], or handheld approaches [15], [16], [17], [18] to overcome the contraints posed by heavy positioning equipment.

Alternatively, the computational imaging (CI) paradigm was introduced aiming to achieve a significant reduction of both the required number of TX-RX channels and the overall acquisition time of the system [4], [19]. For this purpose, CI-based systems generate a set of quasi-orthogonal radiation patterns, or measurement modes, to illuminate the scene under inspection and compress its information into a single channel (or a reduced number of them). The compressive antennas capable of generating the required measurement modes can be found under different implementations, although in the remainder of the manuscript only those based on metasurface antennas will be considered due to their reduced form factor and ease of manufacturing. Metasurface-based antennas for CI can be classified into three main groups depending on how they generate the different radiation patterns required to probe the scene under investigation: (i) through frequency diversity [20], (ii) by means of a dynamic reconfigurability of the antenna aperture [21], or (iii) a combination of both [22]. In frequency diverse antennas the different measurement modes are a set of frequency dependent radiation patterns which ideally are orthogonal to each other [23], [24]. In contrast, a dynamic metasurface antenna (DMA) generates the different radiation patterns by turning on and *off* the radiating elements that populate the antenna aperture by means of a tunable element such as a diode [21]. The use of a DMA or a hybrid approach enables a reduced frequency bandwidth when compared to frequency diverse antennas, which in turn do not require the use of additional tunable elements nor a control circuit to turn them *on* and *off*.

From a hardware perspective, current research efforts in CI systems are devoted to increase the number of measurement modes. As an example, for frequency-diverse antennas, this has been achieved by mechanically rotating a frequency-polarization sensitive metasurface fed by a patch antenna [25] (in order to consider different rotation angles with respect to the feeding patch). In dynamic reconfigurable antennas, the

This work has been partially supported by the Leverhulme Trust through Research Leadership Award under Grant RL-2019-019, and by the UKRI Postdoctoral Fellowship Guarantee for MSCA PF under Project EP/X022943/1 and Project EP/X022951/1.

María García-Fernández, Guillermo Álvarez-Narciandi, and Okan Yurduseven are with the Centre for Wireless Innovation, Queen's University Belfast, United Kingdom (e-mail: {m.garcia-fernandez, g.alvarez-narciandi, okan.yurduseven}@qub.ac.uk).

Manuscript received XX, 2023; revised XX, 2023.

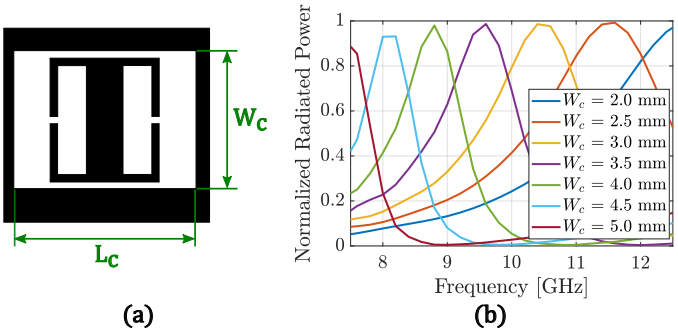

Fig. 1. (a) cELC unit cell design (black colour denotes copper, whilst white regions show etched areas), and (b) normalized radiated power for different values of the unit cell width.

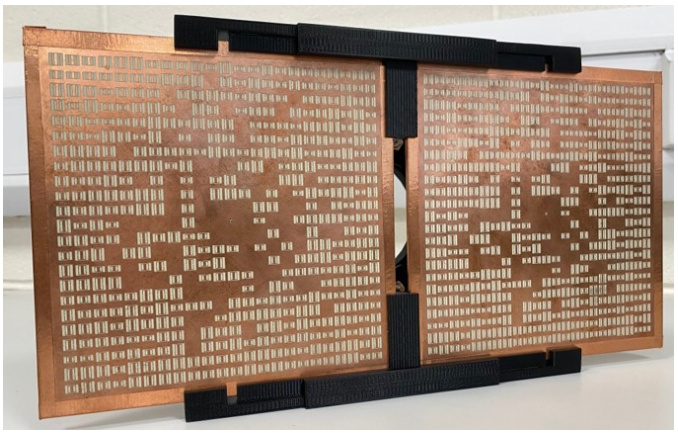

Fig. 2. Picture of the fabricated frequency diverse metasurface antennas.

number of measurement modes has been augmented by resorting to dual-polarized antennas [26] (enabling polarimetric CI), or by using varactors as tuning elements [27]. All these approaches, either relying on mechanical rotation, mechanical movement and/or dynamic reconfigurability, increase the hardware complexity with respect to conventional frequency-diverse antennas. From a software perspective, recent works are particularly focused on improving the efficiency of the imaging algorithms (e.g., applying a decompression step to perform the reconstruction in the frequency domain for 1D DMAs [28][29]) and on leveraging machine learning (e.g., to achieve super-resolution [30]). Nevertheless, it should be highlighted that all these works deal with free-space scenarios.

Regardless of the considered electromagnetic imaging approach, the inspection of an area behind or inside dielectric media (e.g., through-the-wall imaging (TWI) or ground penetrating radar (GPR)) entails additional challenges to the image reconstruction process, namely extra clutter from the reflection produced at the interface between the different media, a shift in the target position and a widening of the point spread function (PSF) along the cross-range direction [31]. Nonetheless, a great research effort has been carried out to improve the quality of the images retrieved by conventional SAR imaging systems in the context of both TWI [32], [33], [34], [35], [36], [37] and GPR [8], [9], [38]. However, the use of CI-based systems in the context of TWI and GPR remains vastly understudied [39], [40], [41], [42]. In [39], a pair of 1D DMAs is used to perform 2D TWI, i.e., a 3D reconstruction is not enabled. Alternatively, in [40], [41], [42] some preliminary studies based on simulations are presented. Besides comprising only simulation results, in these cases the sensing matrix that characterizes the CI system is computed considering a free-space forward model [43]. This is a significant limitation when dealing with realistic walls and can fail to reconstruct the hidden targets.

The main novelties and contributions of this work are summarized as follows:

1) Development of a frequency-diverse antenna at X band, specifically designed for through-the-wall CI. Most CI systems employ antennas at K band, as their targeted application solely involves wave propagation in free-space, such as personnel screening. However, in this work, a lower frequency band has been considered for the development of the compressive antenna to improve the penetration into dielectric media, specifically through-the-wall. The proposed CI antennas do not include any tuning elements, leading to a reduced hardware complexity as they require only a simple frequency sweep to acquire enough information to retrieve an image of the inspected scene.
2) Development of a mathematical model for through-the-wall CI, including the following features:
   a) Contrary to common (free-space) CI models, the proposed model incorporates a backpropagation approach based on solving an inverse problem to estimate an equivalent magnetic current distribution in the antenna aperture. This, in turn, makes possible to consider scenarios where walls are placed at any given distance from the antennas (i.e., not only further than the characterization plane).
   b) The model also takes into account the propagation through-the-wall by resorting to a 3D ray-tracing procedure based on the Snell's law. This enables to obtain well-focused images of the hidden targets at their actual position.
3) Experimental validation of the first frequency-diverse through-the-wall CI system considering different types of wall and different target positions. This constitutes the first practical demonstration of through-the-wall CI relying entirely on frequency-diversity to synthesize quasi-orthogonal radiated field patterns, demonstrating the ability of retrieving 3D radar images from a single acquisition (i.e., frequency sweep).

This work proposes to use frequency diverse antennas to perform through-the-wall sensing. This approach, based on the CI paradigm, allows to retrieve images of the inspected scenario using only a single standalone acquisition, drastically reducing the inspection time compared to conventional radar systems (where the inspected scene must be sampled fulfilling the Nyquist criterion). Furthermore, a processing method to account for the propagation through the wall and to mitigate the wall reflection has been derived. The designed and fabricated frequency diverse antennas, as well as the proposed processing

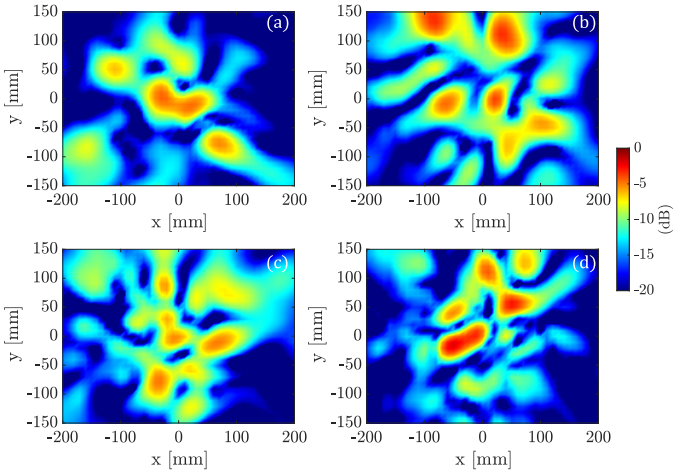

Fig. 3. Measured field magnitude of one the fabricated frequency diverse panels at (a) 9.15 GHz, (b) 10.15 GHz, (c) 11.15 GHz, and at (d) 12.15 GHz. The spatial diversity of the radiated fields versus frequency is evident.

techniques, have been experimentally validated. Results show the feasibility of imaging targets behind different types of wall using a frequency diverse CI system. Furthermore, the developed processing techniques enable improved quality images, facilitating the detection of targets.

The manuscript is organized as follows. The proposed system is described in Section II. This section comprises the design of the frequency diverse antennas and the system architecture, as well as the derivation of the through-the-wall CI reconstruction algorithm. Section III is devoted to the experimental validation of the proposed system. Finally, the main conclusions are drawn in Section IV.

II. Description of the System

In this Section, the design of the fabricated 2D frequency diverse metasurface antennas used for CI and the architecture of the overall system are presented, and the processing algorithms are discussed.

A. Two-dimensional frequency diverse metasurface antennas

As previously introduced, frequency diverse antennas for CI produce a set of quasi-orthogonal radiation patterns as a function of frequency. The antennas presented in this work are two 2D metasurface panels of $15.2\,\text{cm} \times 15.2\,\text{cm}$ size fed by one central port. Although the majority of 2D metasurface antennas for CI operates at K-band (as they are used in personnel screening applications), these antennas have been designed at X-band to improve the penetration through the walls. Each of them is populated by a set of complementary electric inductive-capacitive (cELC) unit cells randomly distributed across the aperture. The cELC unit cells share the same design, depicted in Fig. 1(a), and occupy an area of $6\,\text{mm} \times 6\,\text{mm}$. Their length L_c is set to 5 mm, but their width, W_c, is different from cell to cell. As a consequence, the peak of the power radiated by each unit cell is shifted in frequency. This can be seen in Fig. 1(b), where the power radiated by the unit cell for different values of W_c across the frequency band considered in this work is depicted. These results, which were obtained with a commercial full-wave electromagnetic solver, show that considering unit cells with $W_c \in [2, 5]$ mm, the whole $[7.5, 12.5]$ GHz band can be covered. The random distribution of the cells across the aperture, both in terms of position and of the value of W_c (which, in turn, determines the cell radiating frequency), contributes to obtain the required quasi-orthogonal radiation patterns.

Two units of the metasurface panel were fabricated using a copper-plated Rogers TMM3 substrate of 3.175 mm thickness, with permittivity $\varepsilon_r = 3.45$ and loss tangent of $\tan\delta = 0.002$. Both panels are arranged side by side as depicted in Fig. 2, and the distance between their centers (i.e., their feeding ports) is 16 cm. In this configuration one panel acts as transmitter, whilst the other acts as receiver, i.e., only one radiofrequency channel is considered.

It should be noted that some cells have been removed in the central area of the panels to avoid most of the power being radiated by the cells closer to the feeding port. These cells have been randomly removed, with a probability of removal inversely proportional to the distance to the feeding port. Furthermore, the edges of the antennas have been covered with copper tape to avoid leakage.

The electric near-field (NF) radiated by each of the panels was measured in a planar range antenna measurement facility at 401 equally spaced frequency points in the $[7.5, 12.5]$ GHz frequency band. As it will be explained in Section II-B, an accurate characterization of the antennas is key to enable CI. The magnitude of the measured field radiated by one of the prototypes at four different frequencies is depicted in Fig. 3. As can be seen, the NF radiated by the fabricated antennas differs greatly from the field radiated by conventional antennas. Instead of a well-defined main beam in a fixed direction, there are several beams pointing at different directions. In addition, it should be remarked that the NF changes significantly from frequency to frequency, as required in a frequency diverse antenna to enable CI. To further illustrate how the radiation patterns change with frequency, the correlation coefficient [44] of the measured electric NF among the different frequencies is shown in Fig. 4 for both the fabricated antennas. The closer this correlation matrix to the identity matrix is, the higher the uncorrelation among the different radiation patterns is. Thus, as can be observed in Fig. 4, the radiation patterns are highly uncorrelated among the different frequencies.

Finally, the architecture of the overall system is depicted in Fig. 5. The two frequency diverse panels are placed in front of the wall to be inspected, and are connected to a measurement device (e.g., a vector network analyzer). The ultimate goal is to retrieve an image of the hidden targets (placed behind the wall). A great advantage of the proposed system is that, in order to obtain this image, only a single standalone acquisition is required.

B. Through-the-wall computational imaging reconstruction algorithm

1) Antenna characterization: In conventional radar imaging, a significant number of reconstruction algorithms, such as

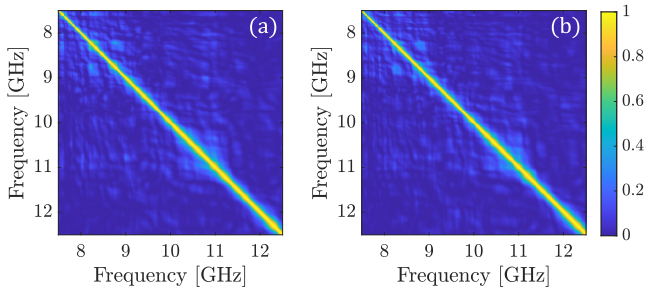

Fig. 4. Correlation of the measured electric NF among the different frequencies for the two frequency diverse fabricated antennas. (a) TX panel, and (b) RX panel.

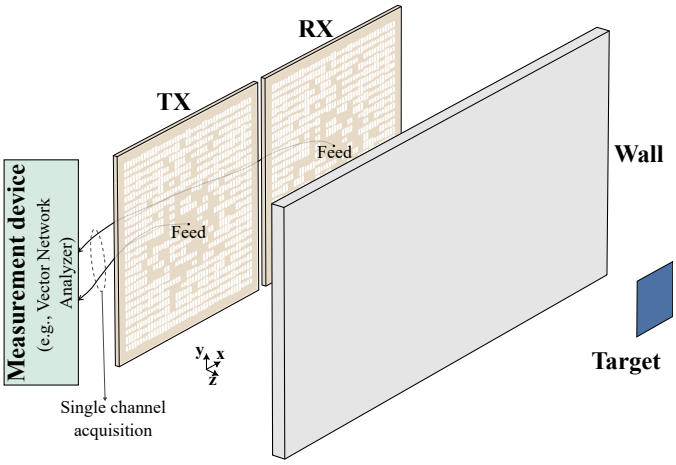

Fig. 5. Architecture of the proposed frequency diverse through-the-wall computational imaging system

those based on Delay-and-Sum [45] or Range Migration [46], do not take into account the antenna radiation pattern (i.e., an isotropic radiation is assumed). However, in CI systems the characterization of the compressive antennas plays a major role, as the radiation patterns are required to retrieve the radar images. This is because compressive antennas radiate quasi-orthogonal (spatially-incoherent) radiation patterns, whereas the antennas used in conventional radar imaging usually exhibit a well-defined main beam in a fixed direction.

Assuming the antenna aperture is placed in the xy-plane (pointing towards the $+z$-axis), an equivalent model of the antenna can be obtained applying the equivalence principle and image theory [47], [48]. In particular, if the antenna is measured in an infinite plane S (at $z = z_s$ and enclosing the radiating sources), an equivalent magnetic current $\boldsymbol{M_{eq}}$ can be estimated as:

$$\boldsymbol{M_{eq}} = -2\hat{\boldsymbol{n}} \times \boldsymbol{E}_s, \tag{1}$$

where $\hat{\boldsymbol{n}}$ is the unit vector normal to S and $\boldsymbol{E}_s$ is the electric field on S. Therefore, $\boldsymbol{M_{eq}}$ is proportional to the tangential electric field and radiates the same fields as the original radiating sources for all points in the region $z > z_s$. In practice, the measurement plane is truncated to a finite size plane S', which limits the region in which the fields can be accurately computed.

Once $\boldsymbol{M_{eq}}$ is estimated, the electric field in a point $\boldsymbol{r}$ can be obtained as:

$$\begin{aligned}\boldsymbol{E}(\boldsymbol{r}) &= -\frac{1}{4\pi}\iint_{S'} \nabla \times \left[\boldsymbol{M_{eq}}(\boldsymbol{r'})\frac{e^{-jkR}}{R}\right] dS' \\ &= \frac{1}{4\pi}\iint_{S'} [\hat{\boldsymbol{R}} \times \boldsymbol{M_{eq}}(\boldsymbol{r'})]\left(\frac{1+jkR}{R^2}\right) e^{-jkR} dS',\end{aligned} \tag{2}$$

where $\nabla\times$ denotes the curl or rotor operator, $\boldsymbol{r'}$ are the points belonging to S', k is the wavenumber in free-space, $R = \|\boldsymbol{r} - \boldsymbol{r'}\|$ and $\hat{\boldsymbol{R}} = \frac{\boldsymbol{r}-\boldsymbol{r'}}{R}$.

2) Free-space CI system modeling: The forward model that relates the backscattered radar measurements ($\boldsymbol{g}$) and the reflectivity of the imaged scene ($\boldsymbol{\rho}$) is given by:

$$\boldsymbol{g}_{M\times 1} = \boldsymbol{H}_{M\times N}\boldsymbol{\rho}_{N\times 1} + \boldsymbol{n}_{M\times 1}, \tag{3}$$

where M is the number of measurement modes (i.e., the number of measured frequency points, which in this case is $M = 401$), N is the number of voxels in the imaged scene, $\boldsymbol{H}$ is the sensing matrix that characterizes the CI system and $\boldsymbol{n}$ is the system noise. It should be noted that in the case of frequency-diverse antennas, the number of measurement modes corresponds to the number of measured frequency points.

Under the first Born approximation, the sensing matrix is given by the dot product between the electric fields of the Tx and Rx antennas projected to the imaged scene [43], i.e.,

$$\boldsymbol{H} = \boldsymbol{E}_{Tx} \cdot \boldsymbol{E}_{Rx}. \tag{4}$$

In the literature, these projected fields are obtained applying (2) for each point $\boldsymbol{r}$ in the imaged scene. Furthermore, they consider that the equivalent magnetic current $\boldsymbol{M_{eq}}$ is given by (1), where $\boldsymbol{E}_s$ is the electric field measured in a NF plane parallel to the antenna aperture and at a given distance from it (typically at several wavelengths) [43]. This means that backpropagation is not considered, thus restricting the applicability to scenarios or targets located further from the antennas than the NF plane. This NF plane is sampled at $\lambda_{\text{min}}/2$ (where λ_{min} is the smallest wavelength, corresponding to the highest frequency).

3) Through-the-wall CI system modeling: As the targeted application of this system is through-the-wall imaging, the computation of the sensing matrix should be modified to account for the propagation through the wall.

The first step consists of estimating an equivalent magnetic current on the antenna aperture. This is accomplished by solving the inverse problem arising from (2) [49], [50]. In particular, assuming the electric field is measured in a plane in the NF region ($\boldsymbol{E}^{\text{NF}}$), the goal is to estimate $\boldsymbol{M_{eq}}$ in a plane tangential to the antenna aperture S' (enclosing the antenna), as illustrated in Fig. 6. According to (1), $\boldsymbol{M_{eq}} = M_{eq,x}\hat{x} + M_{eq,y}\hat{y}$ and the equations corresponding to the $x-$ and $y-$components of the electric field in (2) are decoupled, yielding:

$$\begin{aligned}\begin{bmatrix} E_x^{\text{NF}}(\boldsymbol{r}) \\ E_y^{\text{NF}}(\boldsymbol{r}) \end{bmatrix} &= \frac{1}{4\pi}\iint_{S'} \begin{bmatrix} 0 & -\hat{R}_z \\ \hat{R}_z & 0 \end{bmatrix} \begin{bmatrix} M_{eq,x}(\boldsymbol{r'}) \\ M_{eq,y}(\boldsymbol{r'}) \end{bmatrix} \\ &\cdot \left(\frac{1+jkR}{R^2}\right) e^{-jkR} dS',\end{aligned} \tag{5}$$

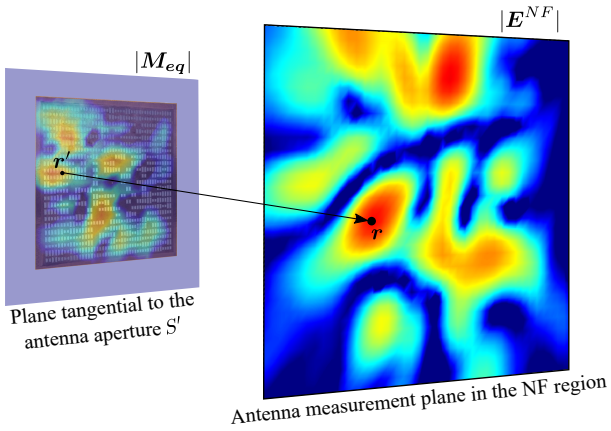

Fig. 6. Illustration of the backpropagation step.

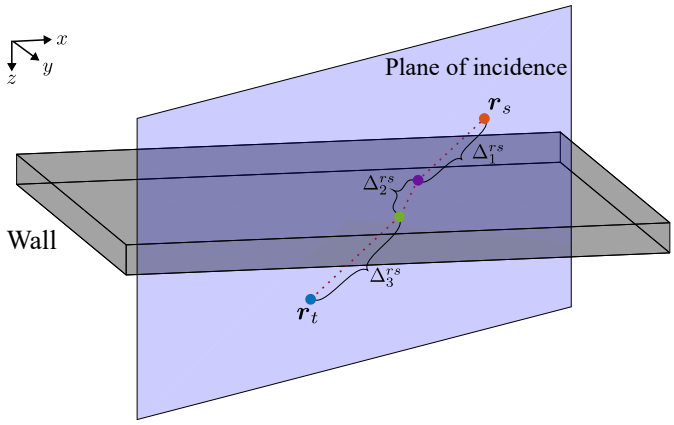

Fig. 7. Scheme of the ray tracing approximation.

where $\hat{R}_z$ is the z-component of $\hat{\boldsymbol{R}}$.

The system of equations obtained from discretizing (5) for all points $\boldsymbol{r}$ where the electric NF is measured and all points $\boldsymbol{r'} \in S'$ is solved using least squares to estimate $\boldsymbol{M_{eq}}$. Then, the electric field in a plane in front of the wall surface, $\boldsymbol{E}_{fw}$, is computed using (2). In order to compensate for the propagation through the wall, the electric field in a plane placed between the antennas and the wall is needed. Therefore, this backpropagation step is essential as the wall under inspection might be closer to the antennas than the NF plane where the electric field was measured.

The next step aims to take into account the refraction of the electromagnetic waves when they impinge on the wall. The approach followed is based on defining a virtual magnetic current on a plane placed behind the wall. This virtual magnetic current aims to model the radiation of the antennas and the propagation through the wall. To compute it, the electric field in the plane in front of the wall ($\boldsymbol{E}_{fw}$) is propagated to each point $\boldsymbol{r}_t$ in the plane behind the wall using ray tracing as follows:

$$\boldsymbol{E}_{bw}(\boldsymbol{r}_t) = \sum_{s=1}^{N_s} \boldsymbol{E}_{fw}(\boldsymbol{r}_s) \frac{e^{-j(k\Delta_1^{rs} + k_{wall}\Delta_2^{rs} + k\Delta_3^{rs})}}{\Delta^{rs}}, \quad (6)$$

where $\boldsymbol{r}_s$ $(s = 1, ..., N_s)$ are the points belonging to the plane in front of the wall, and k_{wall} is the wavenumber in the wall. Δ_1^{rs}, Δ_2^{rs} and Δ_3^{rs} are the distances traveled by a ray propagating from $\boldsymbol{r}_s$ to $\boldsymbol{r}_t$ (in particular, between $\boldsymbol{r}_s$ and the wall front face, inside the wall, and between the wall back face and $\boldsymbol{r}_t$, respectively), and Δ^{rs} is the total distance traveled between $\boldsymbol{r}_s$ and $\boldsymbol{r}_t$.

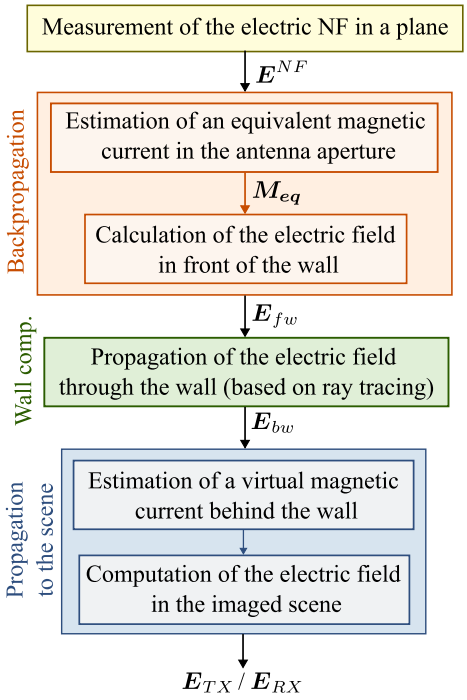

Fig. 8. Scheme of the through-the-wall CI system modeling.

The ray tracing procedure is illustrated in Fig. 7, and the computation of the distances traveled by the ray is based on the Snell's law (applied in the plane of incidence, which is the plane perpendicular to the wall and containing $\boldsymbol{r}_s$ and $\boldsymbol{r}_t$).

The virtual magnetic current is computed according to (1) with $\boldsymbol{E}_s = \boldsymbol{E}_{bw}$ (i.e., the estimated electric field behind the wall). Finally, the electric field is estimated in the imaged scene using (2). This whole procedure, which is summarized in the flowchart shown in Fig. 8, is conducted for both the TX and RX antennas to obtain $\boldsymbol{E}_{TX}$ and $\boldsymbol{E}_{RX}$ and, as a result, retrieve the sensing matrix applying (4).

In this work, the permittivity of the wall is estimated from [51] taking into account the type of material composing the wall. Future work is devoted to estimate the wall parameters from the measurements.

4) Image reconstruction: In order to accurately image the targets hidden behind a wall, besides compensating the refraction due to the presence of the wall, another major issue should be addressed: the clutter caused by the reflections in the wall. To mitigate the reflections from the wall, which in most cases mask the reflection from hidden targets, an average subtraction technique is adopted. This technique consists of averaging N_{av} measurements to estimate the wall response as:

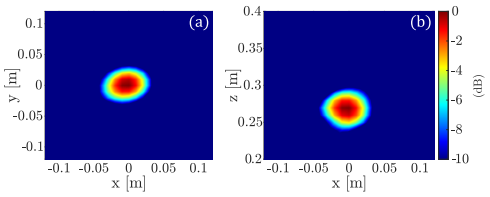

Fig. 9. Reconstruction of a point scatterer (PSF): (a) XY cut and (b) XZ cut. The backscattered signal has been simulated from the measured electric fields.

$$\boldsymbol{g}_{wall} = \frac{1}{N_{av}} \sum_{n_m=1}^{N_{av}} \boldsymbol{g}_{n_m} \tag{7}$$

This estimation of the wall response is subtracted from the backscattered radar measurement before applying the image reconstruction algorithm, i.e., $\boldsymbol{g} = \boldsymbol{g}_{meas} - \boldsymbol{g}_{wall}$.

To estimate the reflectivity of the scene $\boldsymbol{\rho}_{est}$, a least squares approach has been adopted. In particular, $\boldsymbol{\rho}_{est}$ is obtained by minimizing the cost function given in (8), where $\|\cdot\|$ is the Euclidean norm.

$$\boldsymbol{\rho}_{est} = \arg\min_{\boldsymbol{\rho}} \|\boldsymbol{g} - \boldsymbol{H}\boldsymbol{\rho}\|_2^2 \tag{8}$$

5) Point Spread Function (PSF) analysis: In order to analyze the spatial resolution of the system, the PSF has been studied. For this purpose, the backscattered signal from a point scatterer (placed at $x = y = 0\,\text{m}$, and $z = 0.27\,\text{m}$ from the antennas) has been simulated considering the measured electric fields of the fabricated antennas and applying the forward model stated in 4. Two main cuts (XY and XZ) of the reconstructed image, i.e., of the resulting PSF, are shown in Fig. 9. Hence, the spatial resolution of the proposed CI system can be estimated as the width of the PSF at half of its maximum value (known as the Full Width at Half Maximum, FWHM) in the three main axis, yielding: $\delta_x = 0.058\,\text{m}$, $\delta_y = 0.047\,\text{m}$, and $\delta_z = 0.045\,\text{m}$.

The estimated resolution of the proposed frequency-diverse CI system is slightly worse than the resolution expected from a conventional SAR-based imaging system (when considering an aperture with a similar size). However, when using larger apertures (or more TX/RX panels), it has been shown that the resolution achieved with CI is almost the same as with SAR [4].

III. Experimental validation

The capability of the proposed through-the-wall CI system to detect targets hidden behind a wall has been tested for different types of materials. The experimental validation setup is shown in Fig. 10. In particular, the following wall materials and thicknesses have been considered: knotty pine wood ($\varepsilon_r = 1.8$) of 1.8 cm; multilayer plywood with 6 plies ($\varepsilon_r = 2.25$) of 1 cm; chipboard ($\varepsilon_r = 2.7$) of 3.7 cm; and plasterboard ($\varepsilon_r = 2.4$) of 3.75 cm. As aforementioned, the estimations of the wall permittivity ε_r have been extracted from [51], where the complex relative permittivity of common building materials has been measured in the frequency range from 0.2 to 67 GHz.

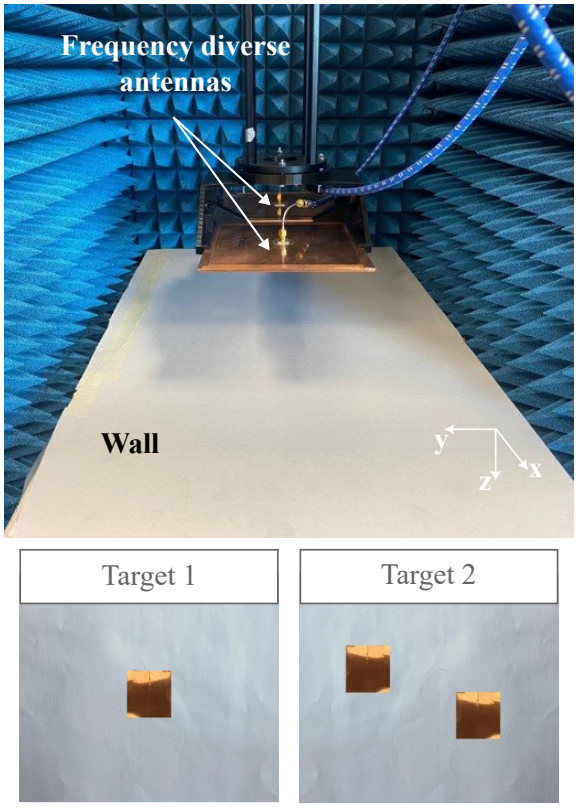

Fig. 10. Setup of the experimental validation. Hidden targets behind the wall are depicted at the bottom.

A. Experiments with a single target

In the first set of experiments, a single target consisting of a 4 cm × 4 cm square patch (made of copper tape) has been considered (target 1 shown in Fig. 10). To facilitate the comparison of the results, the target is placed at the same distance ($z = 27\,\text{cm}$) from the antennas for all the materials. In addition, the back side of the walls is at $z = 15.6\,\text{cm}$ in all the experiments.

The reconstructed images (in the xy plane where the target is placed) are shown in Fig. 11 for three different positions of the target (in the middle and in two positions close to the corners of the imaged scene). The reconstructions of the target without the presence of a wall are also shown as a baseline for comparison in Figs. 11(a)-(c). The rest of the reconstructions correspond to plasterboard (Fig. 11(d)-(f)), plywood (Fig. 11(g)-(i)), knotty pine wood (Fig. 11(j)-(l)), and chipboard (Fig. 11(m)-(o)) walls. Analyzing Fig. 11, it can be concluded that the target is clearly distinguishable in all cases. The reconstructed images when the target is hidden behind a wall are similar to those obtained without the presence of the wall. The main differences are obtained for the wall made of knotty pine wood, Figs. 11(j)-(l), which might be related to the heterogeneity of the pine wood caused by the knots.

It should be highlighted again the benefit of using a CI-based imaging system instead of a conventional SAR system in terms of acquisition time and hardware complexity. In particular, using the proposed system, only a single standalone acquisition is needed to retrieve an image of the inspected

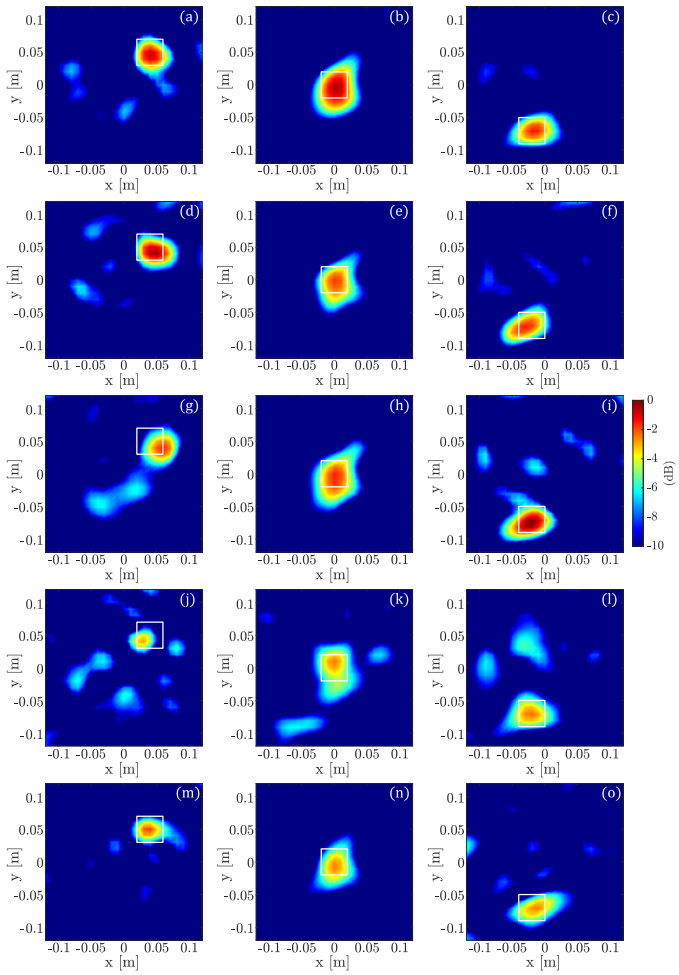

Fig. 11. Reconstructed images of a single target when (a)-(c) no wall is present, and behind a wall made of (d)-(f) plasterboard, (g)-(i) plywood, (j)-(l) knotty pine wood, and (m)-(o) chipboard when the propagation through the wall is accounted for in the processing. Each column corresponds to a different target position, which is depicted with a white square.

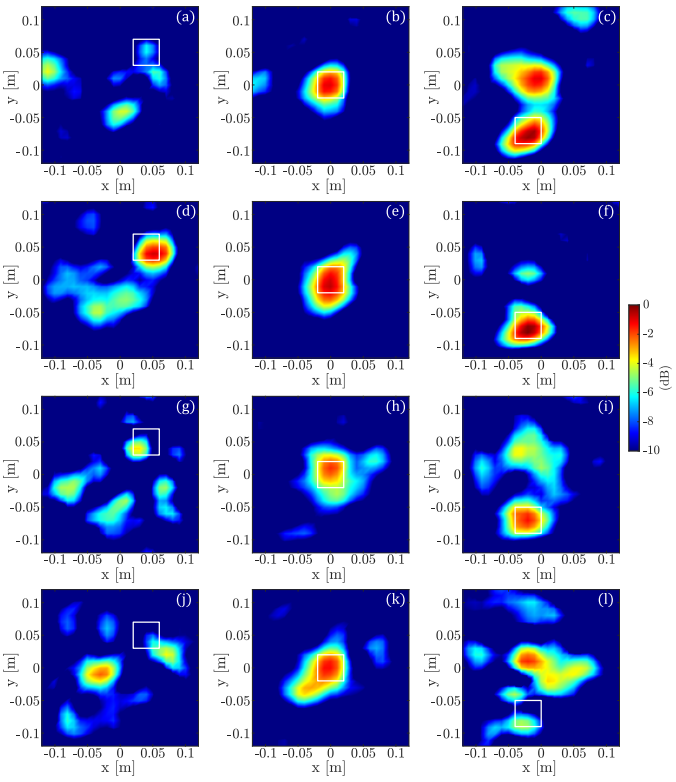

Fig. 12. Reconstructed images of a single target hidden behind a wall made of (a)-(c) plasterboard, (d)-(f) plywood, (g)-(i) knotty pine wood, and (j)-(l) chipboard when the propagation through the wall is not considered in the processing. Each column corresponds to a different target position, which is depicted with a white square.

scene. However, with a SAR-based system $18 \times 18 = 324$ measurement positions would be needed for inspecting an area of $0.2\,\text{m} \times 0.2\,\text{m}$ (which is the region covered by the CI system), as it requires to sample the imaged scene with a $\lambda_{min}/2$ step to satisfy the Nyquist criterion.

In the case of through-the-wall imaging scenarios, an average subtraction technique is employed to mitigate the wall reflection. Nevertheless, in the results shown in this work, only $N_{av} = 10$ measurements are used to estimate the wall response (the measurements gathered with the target placed at the three different positions considered, and seven more measurements with the target placed at a random position behind the wall). Therefore, there is still a drastic reduction in the inspection time compared to a conventional SAR system.

B. Effect of the wall modeling

The procedure explained in II-B to account for the propagation through the wall has been adopted to reconstruct the images shown in Fig. 11. However, it is also of interest to compare these results with the ones obtained when the presence of the wall is not taken into account (that is, when the sensing matrix used in free-space scenarios is considered).

The reconstructed images for the three target positions and the different wall materials when the free-space sensing matrix is used are shown in Fig. 12. As can be seen, there is a clear improvement in the reconstructed images when the sensing matrix with the wall compensation is used (Fig. 11), especially when the target is not located in the middle of the imaged scene. This improvement is particularly noticeable for the walls made of plasterboard and chipboard (because the delay in the propagation of the electromagnetic waves caused by the wall increases with the wall permittivity and thickness). In these cases, the targets in the corners are not detected in the reconstructed images when using the free-space sensing matrix at the location where the targets are placed (see Fig. 12(a), (c), (j), (l)), and there is a significant increase of the clutter of the images.

C. Effect of the wall reflection

As aforementioned, the clutter caused by the reflections of the wall can mask the reflections coming from the hidden targets. Therefore, a clutter mitigation technique, based on averaging a set of N_{av} measurements to estimate the wall has been applied. To illustrate how the detection capabilities deteriorate if the wall reflections are not mitigated, the reconstructed images for the wall made of plasterboard when the clutter reduction technique is not applied are shown in Fig. 13.

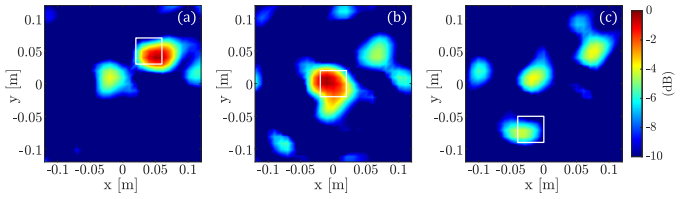

Fig. 13. Reconstructed images of a single target hidden behind a wall made of plasterboard when the propagation through the wall is considered in the processing, but the clutter reduction technique is not applied. Each column corresponds to a different target position, which is depicted with a white square.

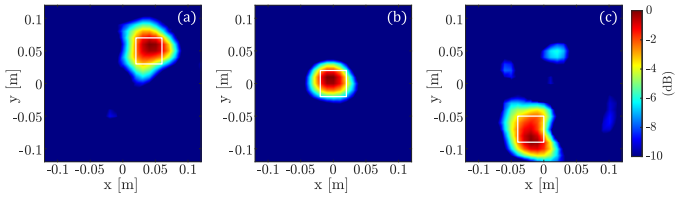

Fig. 14. Reconstructed images of a single target hidden behind a wall made of plasterboard from full-wave simulations. Each column corresponds to a different target position, which is depicted with a white square.

It can be concluded that the quality of the resulting images is significantly deteriorated. Furthermore, in the case of the target placed in the bottom left corner, the clutter level is similar to the reflectivity of the target, thus masking its detection.

D. Comparison with full-wave simulations

It is also worth comparing the reconstructions from the experiments with those obtained from simulations. In particular, a full-wave simulation software has been used to replicate the measurement setup shown in Fig. 10 under ideal conditions. The reconstructed images for the wall made of plasterboard (considering the propagation through the wall in the processing) are shown in Fig. 14 for the three positions of the target. As shown in this figure, the best reconstruction is obtained when the target is placed in the middle of the imaged scene, whereas the clutter level is slightly more noticeable in the reconstructions obtained for the other two target positions. It should be noted that this is in agreement with the results obtained in the experimental campaign (Fig. 11(d)-(f)).

E. Experiments with a distributed target

After assessing the performance of the system for detecting one target hidden behind different types of wall, the capability to detect multiple targets is assessed. In particular, a distributed target composed of two square patches of $4\,\text{cm} \times 4\,\text{cm}$ made of copper tape (whose centers are separated $\Delta_x = 10\,\text{cm}$ and $\Delta_y = 4\,\text{cm}$) has been considered (target 2 shown in Fig. 10). This distributed target is also placed at $z = 27\,\text{cm}$ from the antennas.

The reconstructed images are shown in Fig. 15. Fig. 15(a) shows the image retrieved when there was no wall in the imaging scenario, which serves as a baseline for the other cases with different types of wall. Figs. 15(b), (c), (d), and (e) are the obtained images when the targets were behind a wall made of plasterboard, plywood, knotty pine wood, and chipboard, respectively. As it can be observed, the two targets can be clearly detected and the reconstructed images when the wall is present are similar to the case without a wall. As in the previous experiments (with only a single target), the main differences are observed for the wall made of knotty pine wood.

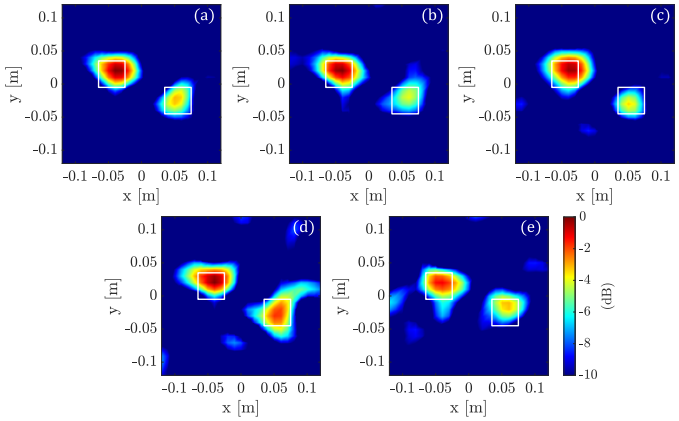

Fig. 15. Reconstructed images of the two square targets (a) in free-space, and behind (b) a plasterboard wall, (c) a plywood wall, (d) a knotty pine wood wall, and (e) a chipboard wall. The targets locations are depicted with white squares.

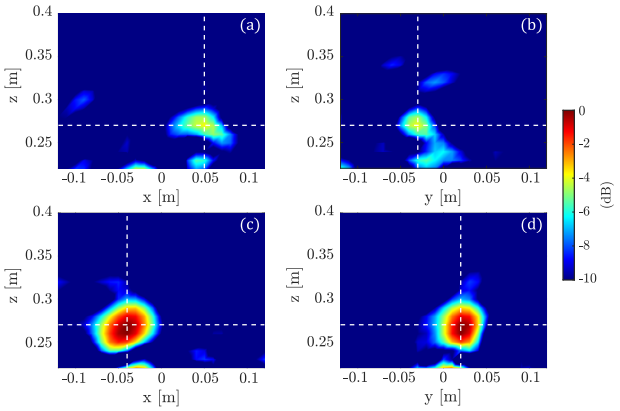

Fig. 16. Reconstructed image of the two square targets behind a plasterboard wall: (a) XZ and (b) YZ planes for the target placed on the right in Fig. 15(b); and (c) XZ and (d) YZ planes for the target placed on the left in Fig. 15(b).

To facilitate the comparison of the results obtained in the different experiments, the reconstructed images have been compared in the XY plane where the targets are located. However, it should be noted that a full 3D reconstruction is retrieved. In Fig. 16 the reconstructed image for the two targets hidden behind the plasterboard wall is shown at the two perpendicular planes intersecting each of the targets. As can be observed in this figure, the two targets can be clearly detected and there is almost no clutter in the reconstructed image.

IV. Conclusions

This manuscript presented a through-the-wall imaging system based on using frequency diverse metasurface antennas.

By relying on CI, the scene information is compressed into a single channel, so only one standalone acquisition is needed to retrieve an image from the scene, which drastically reduces the acquisition time required to retrieve an image from the scene. The results obtained in the experimental validation demonstrated that the proposed system can successfully detect targets hidden behind different types of wall, drastically reducing the number of measurements compared to conventional radar systems (e.g., based on SAR). Furthermore, it was also shown that when the propagation through the wall is accounted for in the processing method, the quality of the resulting images improves notably. This work paves the way to use frequency diverse CI systems for a wide range of through-the-wall sensing applications, allowing a fast inspection of the region of interest.

REFERENCES

[1] M. Pastorino, *Microwave Imaging*. John Wiley & Sons, Inc., 2010.

[2] D. M. Sheen, D. L. McMakin, and T. E. Hall, "Three-dimensional millimeter-wave imaging for concealed weapon detection," *IEEE Trans. Microw. Theory Tech.*, vol. 49, no. 9, pp. 1581–1592, Sep. 2001.

[3] S. S. Ahmed, A. Schiessl, and L. P. Schmidt, "A novel fully electronic active real-time imager based on a planar multistatic sparse array," *IEEE Trans. Microw. Theory Techn.*, vol. 59, no. 12, pp. 3567–3576, Dec 2011.

[4] J. N. Gollub, O. Yurduseven, K. P. Trofatter, D. Arnitz, M. F. Imani, T. Sleasman, M. Boyarsky, A. Rose, A. Pedross-Engel, H. Odabasi, T. Zvolensky, G. Lipworth, D. Brandy, D. L. Marks, M. S. Reynolds, and D. R. Smith, "Large metasurface aperture for millimeter wave computational imaging at the human-scale," *Scientific Reports*, vol. 20, pp. 1–9, Feb 2017.

[5] Z. Wang, T. Chang, and H.-L. Cui, "Review of Active Millimeter Wave Imaging Techniques for Personnel Security Screening," *IEEE Access*, vol. 7, pp. 148 336–148 350, 2019.

[6] D. J. Daniels, "A review of GPR for landmine detection," *Sensing and Imaging: an International Journal*, vol. 7, pp. 90–123, 2006.

[7] E. Schreiber, M. Peichl, A. Heinzel, S. Dill, F. Bischeltsrieder, S. Anger, T. Kempf, and M. Jirousek, "Challenges for operational use of ground-based high-resolution SAR for landmines and UXO detection," in *Proceedings of EUSAR 2016: 11th European Conference on Synthetic Aperture Radar*, 2016, pp. 1–4.

[8] M. García-Fernández, G. Álvarez Narciandi, Y. Álvarez López, and F. Las-Heras Andrés, "Improvements in GPR-SAR imaging focusing and detection capabilities of UAV-mounted GPR systems," *ISPRS Journal of Photogrammetry and Remote Sensing*, vol. 189, pp. 128–142, 2022.

[9] M. García-Fernández, G. Álvarez Narciandi, Y. Álvarez López, and F. Las-Heras, "Array-Based Ground Penetrating Synthetic Aperture Radar on Board an Unmanned Aerial Vehicle for Enhanced Buried Threats Detection," *IEEE Transactions on Geoscience and Remote Sensing*, vol. 61, pp. 1–18, 2023.

[10] S. Kharkovsky, J. T. Case, M. A. Abou-Khousa, R. Zoughi, and F. L. Hepburn, "Millimeter-wave detection of localized anomalies in the space shuttle external fuel tank insulating foam," *IEEE Trans. Instrum. Meas.*, vol. 55, no. 4, pp. 1250–1257, Aug 2006.

[11] J. Laviada, B. Wu, M. T. Ghasr, and R. Zoughi, "Nondestructive Evaluation of Microwave-Penetrable Pipes by Synthetic Aperture Imaging Enhanced by Full-Wave Field Propagation Model," *IEEE Transactions on Instrumentation and Measurement*, vol. 68, no. 4, pp. 1112–1119, 2019.

[12] H. Fernández Álvarez, G. Álvarez Narciandi, M. García-Fernández, J. Laviada, Y. Álvarez López, and F. Las-Heras Andrés, "A Portable Electromagnetic System Based on mm-Wave Radars and GNSS-RTK Solutions for 3D Scanning of Large Material Piles," *Sensors*, vol. 21, no. 3, 2021.

[13] N. K. Nikolova, "Microwave imaging for breast cancer," *IEEE Microwave Magazine*, vol. 12, no. 7, pp. 78–94, Dec 2011.

[14] M. T. Bevacqua, S. Di Meo, L. Crocco, T. Isernia, and M. Pasian, "Millimeter-waves breast cancer imaging via inverse scattering techniques," *IEEE Journal of Electromagnetics, RF and Microwaves in Medicine and Biology*, vol. 5, no. 3, pp. 246–253, 2021.

[15] G. Álvarez-Narciandi, M. López-Portugués, F. Las-Heras, and J. Laviada, "Freehand, Agile, and High-Resolution Imaging With Compact mm-Wave Radar," *IEEE Access*, vol. 7, pp. 95 516–95 526, 2019.

[16] R. Hussung, A. Keil, and F. Friederich, "Handheld millimeter wave imaging system based on a two-dimensional multistatic sparse array," in *2020 45th International Conference on Infrared, Millimeter, and Terahertz Waves (IRMMW-THz)*, 2020, pp. 1–2.

[17] G. Álvarez Narciandi, J. Laviada, and F. Las-Heras, "Freehand mm-Wave Imaging With a Compact MIMO Radar," *IEEE Transactions on Antennas and Propagation*, vol. 69, no. 2, pp. 1224–1229, 2021.

[18] ——, "Towards turning smartphones into mmWave scanners," *IEEE Access*, vol. 9, pp. 45 147–45 154, 2021.

[19] J. Hunt, T. Driscoll, A. Mrozack, G. Lipworth, M. Reynolds, D. Brady, and D. Smith, "Metamaterial apertures for computational imaging," *Science*, vol. 339, no. 6117, pp. 310–313, 2013.

[20] O. Yurduseven, J. Gollub, D. Marks, and D. Smith, "Frequency-diverse microwave imaging using planar mills-cross cavity apertures," *Optics Express*, vol. 24, no. 8, pp. 8907–8925, April 2016.

[21] M. F. Imani, T. Sleasman, and D. R. Smith, "Two-dimensional dynamic metasurface apertures for computational microwave imaging," *IEEE Antennas and Wireless Propagation Letters*, vol. 17, no. 12, pp. 2299–2303, 2018.

[22] T. A. Sleasman, M. F. Imani, A. V. Diebold, M. Boyarsky, K. P. Trofatter, and D. R. Smith, "Implementation and Characterization of a Two-Dimensional Printed Circuit Dynamic Metasurface Aperture for Computational Microwave Imaging," *IEEE Transactions on Antennas and Propagation*, vol. 69, no. 4, pp. 2151–2164, 2021.

[23] O. Yurduseven, V. R. Gowda, J. N. Gollub, and D. R. Smith, "Printed Aperiodic Cavity for Computational and Microwave Imaging," *IEEE Microwave and Wireless Components Letters*, vol. 26, no. 5, pp. 367–369, 2016.

[24] O. Yurduseven, J. N. Gollub, D. L. Marks, and D. R. Smith, "Frequency-diverse microwave imaging using planar Mills-Cross cavity apertures," *Opt. Express*, vol. 24, no. 8, pp. 8907–8925, Apr 2016.

[25] M. Zhao, S. Zhu, H. Huang, D. Hu, X. Chen, J. Chen, and A. Zhang, "Frequency–polarization sensitive metasurface antenna for coincidence imaging," *IEEE Antennas and Wireless Propagation Letters*, vol. 20, no. 7, pp. 1274–1278, 2021.

[26] T. V. Hoang, V. Fusco, T. Fromenteze, and O. Yurduseven, "Dynamic metasurface antenna for computational polarimetric imaging," in *2022 16th European Conference on Antennas and Propagation (EuCAP)*, 2022, pp. 1–5.

[27] A. Diebold, M. Boyarsky, and D. Smith, "A K-band, varactor-tuned dynamic metasurface aperture for microwave computational imaging," in *2023 IEEE Conference on Antenna Measurements and Applications (CAMA)*, 2023, pp. 474–478.

[28] V. Skouroliakou, A. M. Molaei, M. García-Fernández, G. Álvarez Narciandi, and O. Yurduseven, "Frequency Domain Image Reconstruction for Imaging With Multistatic Dynamic Metasurface Antennas," *IEEE Access*, vol. 10, pp. 124 728–124 737, 2022.

[29] A. M. Molaei, T. Fromenteze, S. Hu, V. Fusco, and O. Yurduseven, "Fourier-based near-field three-dimensional image reconstruction in a multistatic imaging structure using dynamic metasurface antennas," *IEEE Transactions on Computational Imaging*, vol. 8, pp. 1089–1100, 2022.

[30] R. Sharma, J. Zhang, R. Kumar, B. Deka, V. Fusco, and O. Yurduseven, "3-D Super-Resolution of Coded Aperture Millimeter-Wave Images Using Complex-Valued Convolutional Neural Network," *IEEE Sensors Journal*, vol. 22, no. 21, pp. 20 921–20 936, 2022.

[31] M. Dehmollaian and K. Sarabandi, "Refocusing Through Building Walls Using Synthetic Aperture Radar," *IEEE Transactions on Geoscience and Remote Sensing*, vol. 46, no. 6, pp. 1589–1599, 2008.

[32] G. Wang and M. Amin, "Imaging Through Unknown Walls Using Different Standoff Distances," *IEEE Transactions on Signal Processing*, vol. 54, no. 10, pp. 4015–4025, 2006.

[33] Y.-S. Yoon and M. G. Amin, "Spatial filtering for wall-clutter mitigation in through-the-wall radar imaging," *IEEE Transactions on Geoscience and Remote Sensing*, vol. 47, no. 9, pp. 3192–3208, 2009.

[34] C. Thajudeen, A. Hoorfar, and W. Zhang, "Estimation of frequency-dependent parameters of unknown walls for enhanced through-the-wall imaging," in *2011 IEEE International Symposium on Antennas and Propagation (APSURSI)*, 2011, pp. 3070–3073.

[35] X. Liu, H. Leung, and G. A. Lampropoulos, "Effect of Wall Parameters on Ultra-Wideband Synthetic Aperture Through-the-Wall Radar Imaging," *IEEE Transactions on Aerospace and Electronic Systems*, vol. 48, no. 4, pp. 3435–3449, 2012.

[36] E. Lagunas, M. G. Amin, F. Ahmad, and M. Najar, "Joint Wall Mitigation and Compressive Sensing for Indoor Image Reconstruction," *IEEE Transactions on Geoscience and Remote Sensing*, vol. 51, no. 2, pp. 891–906, 2013.

[37] F. H. C. Tivive, A. Bouzerdoum, and M. G. Amin, "A Subspace Projection Approach for Wall Clutter Mitigation in Through-the-Wall Radar Imaging," *IEEE Transactions on Geoscience and Remote Sensing*, vol. 53, no. 4, pp. 2108–2122, 2015.

[38] A. Grathwohl, B. Arendt, T. Grebner, and C. Waldschmidt, "Detection of Objects Below Uneven Surfaces With a UAV-Based GPSAR," *IEEE Transactions on Geoscience and Remote Sensing*, vol. 61, pp. 1–13, 2023.

[39] T. Sleasman, M. F. Imani, M. Boyarsky, K. P. Trofatter, and D. R. Smith, "Computational through-wall imaging using a dynamic metasurface antenna," *OSA Continuum*, vol. 2, no. 12, pp. 3499–3513, Dec 2019.

[40] T. V. Hoang, R. Kumar, T. Fromenteze, M. García-Fernández, G. Álvarez Narciandi, V. Fusco, and O. Yurduseven, "Frequency selective computational through wall imaging using a dynamically reconfigurable metasurface aperture," *IEEE Open Journal of Antennas and Propagation*, vol. 3, pp. 353–362, 2022.

[41] G. Alvarez-Narciandi, M. Garcia-Fernandez, and O. Yurduseven, "C-Band Two-Dimensional Dynamic Metasurface Antenna for Through-the-Wall Computational Imaging," in *2023 17th European Conference on Antennas and Propagation (EuCAP)*, 2023, pp. 1–4.

[42] M. Garcia-Fernandez, G. Alvarez-Narciandi, and O. Yurduseven, "Frequency-Diverse Metasurface Antenna for Computational Through-Wall Imaging," in *2023 17th European Conference on Antennas and Propagation (EuCAP)*, 2023, pp. 1–5.

[43] G. Lipworth, A. Rose, O. Yurduseven, V. R. Gowda, M. F. Imani, H. Odabasi, P. Trofatter, J. Gollub, and D. R. Smith, "Comprehensive simulation platform for a metamaterial imaging system," *Applied Optics*, vol. 54, no. 31, pp. 9343–9353, Nov 2015.

[44] J. Thaysen and K. B. Jakobsen, "Envelope correlation in (N,N) MIMO antenna array from scattering parameters," *Microwave and Optical Technology Letters*, vol. 48, no. 5, pp. 832–834, May 2006.

[45] J. Lopez-Sanchez and J. Fortuny-Guasch, "3-D radar imaging using range migration techniques," *IEEE Transactions on Antennas and Propagation*, vol. 48, no. 5, pp. 728–737, 2000.

[46] J. A. Martinez-Lorenzo, C. M. Rappaport, and F. Quivira, "Physical limitations on detecting tunnels using underground-focusing spotlight synthetic aperture radar," *IEEE Transactions on Geoscience and Remote Sensing*, vol. 49, no. 1, pp. 65–70, 2011.

[47] T. K. Sarkar, M. Salazar-Palma, M. D. Zhu, and H. Chen, *The Source Reconstruction Method*, 2021, pp. 235–317.

[48] Y. Alvarez, F. Las-Heras, and C. Garcia, "The sources reconstruction method for antenna diagnostics and imaging applications," in *Solutions and Applications of Scattering, Propagation, Radiation and Emission of Electromagnetic Waves*, A. Kishk, Ed. Rijeka: IntechOpen, 2012, ch. 6.

[49] F. Las-Heras, M. Pino, S. Loredo, Y. Alvarez, and T. Sarkar, "Evaluating near-field radiation patterns of commercial antennas," *IEEE Transactions on Antennas and Propagation*, vol. 54, no. 8, pp. 2198–2207, 2006.

[50] P. Petre and T. Sarkar, "Planar near-field to far-field transformation using an equivalent magnetic current approach," *IEEE Transactions on Antennas and Propagation*, vol. 40, no. 11, pp. 1348–1356, 1992.

[51] S. S. Zhekov, O. Franek, and G. F. Pedersen, "Dielectric properties of common building materials for ultrawideband propagation studies," *IEEE Antennas and Propagation Magazine*, vol. 62, no. 1, pp. 72–81, Feb. 2020.